sustainability

Article

The Influence of SnO_2 and Noble Metals on the Properties of TiO_2 for Environmental Sustainability

Evghenii Goncearenco [1,†], Iuliana P. Morjan [1,†], Claudiu Fleaca [1], Elena Dutu [1], Anca Criveanu [1], Cristian Viespe [1], Aurelian Catalin Galca [2], Adrian Valentin Maraloiu [2], Miruna S. Stan [3], Carmen Ioana Fort [4,*] and Monica Scarisoreanu [1,*]

[1] National Institute for Lasers, Plasma and Radiation Physics, 409 Atomistilor Str., 077125 Magurele, Romania; evghenii.goncearenco@inflpr.ro (E.G.); iuliana.morjan@inflpr.ro (I.P.M.); claudiu.fleaca@inflpr.ro (C.F.); elena.dutu@inflpr.ro (E.D.); anca.criveanu@inflpr.ro (A.C.); cristian.viespe@inflpr.ro (C.V.)
[2] National Institute of Materials Physics, 405A Atomistilor Str., 077125 Magurele, Romania; ac_galca@infim.ro (A.C.G.); maraloiuvalentin@gmail.com (A.V.M.)
[3] Department of Biochemistry and Molecular Biology, Faculty of Biology, University of Bucharest, 91-95 Splaiul Independenţei Str., 050095 Bucharest, Romania; miruna-stan@bio.unibuc.ro
[4] Research Center of Electrochemistry and Non-Conventional Materials, Department of Chemical Engineering, Faculty of Chemistry and Chemical Engineering, “Babes-Bolyai” University, 11 Arany Janos Str., 400028 Cluj-Napoca, Romania
* Correspondence: ioana.fort@ubbcluj.ro (C.I.F.); monica.scarisoreanu@inflpr.ro (M.S.)
† These authors contributed equally to this work.

Abstract: In order to find solutions to current worldwide environmental problems, it is crucial to develop sustainable nanomaterials, ideally with multifunctional properties. Considering this, novel TiO_2-SnO_2@NMs (noble metals: Au and Ag) composites, for use as sustainable nanomaterials, were successfully prepared via a two-step synthesis process consisting of laser pyrolysis followed by the chemical impregnation of the collected materials with noble metals. The addition of SnO_2 favors the transformation of TiO_2 from a mixture with a majority Anatase phase to one with a Rutile phase majority. With consideration for their level of environmental toxicity, the features of the synthesized nanomaterials were structurally, morphologically, and optically described and assessed for environmental protection applications as gas sensors and photocatalysts. In the case of the Surface Acoustic Wave sensor, based on a pure TiO_2 nanopowder, a notable difference in the frequency shift was detected in comparison to the other examined sensors. All sensors responded to the CH_4 concentrations tested (0.02–0.1%). On the other hand, when methyl orange was photodegraded under visible light, the results obtained using NMs for decoration revealed that the photocatalytic activity of TiO_2-SnO_2@NMs was significantly improved compared to the TiO_2-SnO_2 binary composite, which already has an enhanced photocatalytic activity, compared to pure TiO_2. Overall, this work produces nanoparticles that exhibit better sensory and photocatalytic features, as well as higher levels of biocompatibility with skin cells, for use as eco-friendly nanomaterials for a sustainable future.

Keywords: TiO_2-SnO_2@Au/Ag; SAW sensors; photodegradation; biocompatibility; sustainability

Citation: Goncearenco, E.; Morjan, I.P.; Fleaca, C.; Dutu, E.; Criveanu, A.; Viespe, C.; Galca, A.C.; Maraloiu, A.V.; Stan, M.S.; Fort, C.I.; et al. The Influence of SnO_2 and Noble Metals on the Properties of TiO_2 for Environmental Sustainability. *Sustainability* **2024**, *16*, 2904. https://doi.org/10.3390/su16072904

Academic Editors: Paola Verlicchi, Silvia Venditti, Stijn Van Hulle and Marie Launay

Received: 1 March 2024
Revised: 26 March 2024
Accepted: 27 March 2024
Published: 30 March 2024

1. Introduction

Since the 20th century, air and water pollution have been recognized as one of the most urgent issues and the development of environmentally friendly nanomaterials is essential in addressing this issue. Within this context, the multifunctionality of nanomaterials is the key factor which has to be developed in order to be successful in addressing these issues. Enhancing this characteristic of a nanomaterial system, using different means such as defect engineering or doping, can give rise to real solutions to the current environmental problems. The tailoring of the multifunctional properties exhibited by the metal-oxide composite nanoparticle TiO_2/SnO_2 system, such as the catalytic and sensing properties, as well as the biocompatible ones, is targeted within this study.

In order to prevent air pollution, monitoring combustible gases in the workplace is essential for the purpose of preventing accidents like industrial and mining explosions. The most widely used gas is methane (CH_4), which is a key component of natural gas and is used as a long-range energy source for both home and industrial applications, also being the second most important greenhouse gas. It is a colorless, odorless, and flammable gas that can cause asphyxia by decreasing the O_2 percentage in a closed room and can cause explosions at relative low concentrations in the air (~4.7–15.5 vol. %) [1]. Therefore, it is crucial to understand how to effectively detect and monitor CH_4 using a simple and practical approach in order to reduce health hazards and ensure human safety in both industrial and domestic areas [2]. Because most metal oxide-based sensors work at high temperatures, they are expensive and have a short durability [3]. For these reasons, it is crucial to create CH_4 sensors based on semiconductor metal oxide (SMO) materials such as TiO_2 or SnO_2 [1]. Since Fujishima et al. noticed the photocatalytic splitting of water on a titanium dioxide (TiO_2) electrode under the irradiation of UV light in 1972 [4], TiO_2 has received a lot of interest as a semiconductor metal oxide. Moreover, TiO_2 and SnO_2 are semiconductor oxides that are often used in the field of gas/vapor sensing for different types of sensors for gases [5,6]. Surface Acoustic Wave (SAW) sensors stand out for their good sensitivity, stability, fast response, and the possibility of wireless operation. Their operating principle is based on changing the oscillation frequency of the wave front that crosses the sensor when the sensitive layer undergoes a change, due to the gas molecules present on its surface [7]. Thus, for this type of sensor, the characteristics of the sensitive layer directly influence the sensor results. It has been demonstrated that the greater the specific surface area of the film, the greater the sensitivity of the sensor [8]. Consequently, the use of nanoparticles (NPs) or porous layers in the production of SAW sensors leads to an improvement in their performances.

In order to prevent water pollution, the decontamination of wastewater is also an important aspect, due to its negative consequences on the environment and human health. In this context, significant research efforts have been made to discover new materials sensitive to solar light that can clean wastewater by producing highly reactive hydroxyl radicals that break down dissolved organic pollutants and, subsequently, transform them to non-toxic chemicals. Due to their distinctive catalytic capabilities and their broad variety of uses, metal oxides such as TiO_2, ZnO, or SnO_2 have attracted a lot of attention in the field of nanotechnology [9]. The most utilized photocatalytic material is TiO_2, which reacts strongly to UV light (387 nm), having low toxicity, as well as excellent thermal and chemical stability. Due to these reasons, TiO_2 materials are used in a variety of industries, such as the chemical, pharmaceutical, and food industries, among others [9–11]. The Anatase crystalline phase of TiO_2 is typically preferred because of its strong oxidation activity, which can harness energy above the band gap of 3.3 eV [4,10], its ability to produce both electrons and holes when exposed to sunlight, and its low recombination rates of these charge carriers [9]. By doping with metallic or non-metallic elements, its catalytic activity can be enhanced. These dopants, as well as interstitial and substitutional defects, can be introduced into the host lattice sites. The bandgap energy is decreased as a result of this impact and its electronic characteristics are enhanced. The recombination rate of electrons and holes is also influenced by doping and defect generation, which has an impact on the performance of the catalytic system. The most popular dopants for titania are zinc and tin [9], because these doped materials have more tunable properties than bare TiO_2, such as durability and improved interaction with organic dyes, as well as promising activity in the UV and visible spectrum ranges. Due to the increased generation of hydroxyl radicals, SnO_2 is crucial in structural nanocomposites with TiO_2 [11,12]. On the other hand, the scientific community has developed an intense interest in Au clusters and photocatalysts based on nanoparticles, with particular focus on their use in dye degradation. Due to their surface plasmon resonance (SPR) effects, Au and Ag nanoparticles are chosen over many other plasmonic or semiconductor composite materials due to their stability, non-toxicity, and biocompatibility. The efficiency of the semiconductor surface can be improved by increasing the absorption of organic dyes, extending light absorption into the visible range, and maintaining efficient charge separation/carrier transport to the photocatalyst surface, as demonstrated for a variety of TiO_2 nanostructures loaded with Au/Ag NPs [13,14]. Dye pollution from the paper, tanning, cosmetic, textile, and paint industries represents a significant proportion of the overall water pollution. Dyes are used in several industries due to their characteristics including their distinct structural features, chemical stability, various functional groups, and distinctive colors (methyl orange and methylene blue) [15]. methyl orange (MO) (an azo dye), as well as methylene blue (a thiazine dye), can be found in many wastewaters and are harmful to both aquatic and human life. Due to the stability of these dyes and their byproducts, which are mutagenic and carcinogenic in nature, they are more harmful than other organic dyes. Methods involving conventional biological degradation are not suitable for these dyes, since they are very difficult to biodegrade. With the help of nanoparticles, photocatalytic degradation is a commonly utilized technique for the destruction of harmful dyes in water [14,16].

In one of our previous studies, we followed the MO photodegradation process under UV–Vis light using TiO_2-SnO_2 nanopowders with different concentrations of Sn (1.1–4.8 at.%), the best results being obtained for the sample with the highest tin concentration ($k = 9.6 \times 10^{-3}$ min^{-1}) [17]. Other results from our research demonstrated that simple TiO_2 nanoparticles decorated with Ag were able to completely and more quickly ($k = 16.78 \times 10^{-3}$ min^{-1}) photodegrade MO under Vis light [18].

The objective of this study was to tailor the photocatalytic properties of TiO_2-SnO_2 nanopowders, in connection with CH_4 sensing capabilities and superior biocompatible properties, as targeted multifunctionalities for this nanoparticle system. To this end, we have obtained TiO_2-SnO_2 nanopowders with a higher Sn concentration than in previous studies, also assisted by the NM decoration of these nanoparticles, in order to achieve the photodegradation process using Vis light. The nanomaterials investigated in the photodegradation process were examined for sensor applications in the detection of CH_4 gas within a SAW device configuration. The last important objective of this study was to evaluate the cytotoxicity of P25 and TiO_2-SnO_2@NMs nanoparticles on HaCaT cells, which are widely accepted as a relevant and suitable model for human skin cells. By utilizing this cell line, which possesses similar characteristics to normal human epidermal keratinocytes, we can gain valuable insights into the potential adverse effects of the TiO_2-based nanoparticles commonly used in various skin applications, such as sunscreen formulations, cosmetic products, anti-aging creams, and wound healing materials. Our findings will contribute to a better understanding of the cytotoxicity of these newly developed nanoparticles on human skin cells, providing important insights for their safe utilization.

2. Materials and Methods

2.1. Synthesis of TiO_2-SnO_2 Nanopowders

In our previous research, we described how pure or doped TiO_2 nanoparticles can be synthesized in a bottom-up approach using the laser pyrolysis (LP) method. The basic concept behind the LP process, which can be used to create a variety of nanoparticles, is the interaction of an IR laser beam ($\lambda = 10.6$ µm) with a mixture of gaseous or liquid precursors. In the current study, a CW CO_2 laser (P = 390 W) was used and a mixture consisting of ethylene as a sensitizer ($\Phi_{C2H4} = 70$ sccm—absorbs the laser radiation and transfers its energy through collisions to the precursor molecules), vapors from $TiCl_4$ and $SnCl_4$ volatile anhydrous liquids ($\Phi_{Air\rightarrow TiCl4} = 90$ sccm, $\Phi_{Air\rightarrow SnCl4} = 20$ sccm—as precursors for titanium and tin atoms), and synthetic air ($\Phi_{Air} = 450$ sccm—which plays the role of oxidizing agent in the LP flame and also of carrier gas for the vapors provided by the liquid precursors). The Ar flow for the gas precursors' confinement and the pressure in the reaction chamber were kept constant, at 2000 sccm and 450 mbar, respectively. A vertical injector with two concentric nozzles was used for the introduction of gas/vapors into the reaction chamber, as shown in Figure 1.

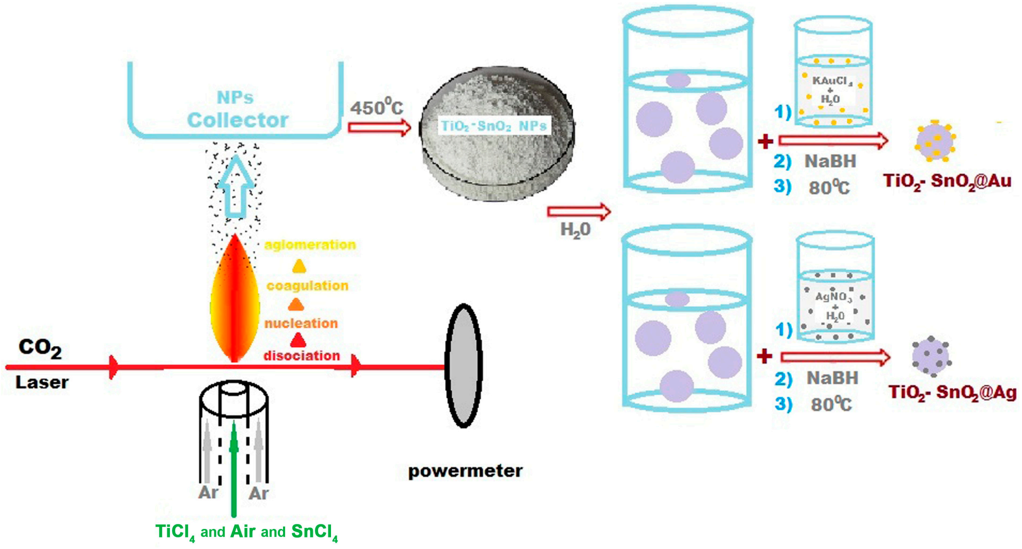

Figure 1. The process of obtaining TiO_2-SnO_2@Au/Ag nanomaterials.

Two samples of nanopowders representing pure TiO_2 and TiO_2-SnO_2, respectively, were obtained after the pyrolysis process. These samples were calcined at a temperature of 450 °C for 3 h to remove any potential C or "butter of tin" ($SnCl_4{\cdot}5H_2O$) impurities, being labeled as T and TS, respectively. Noble metal decoration was produced by chemical impregnation (CI) of TS nanoparticles with two aqueous solutions of noble metal precursors, as follows: $AgNO_3$ (Chemical Company, Iasi, Romania, 99.5% purity) and $KAuCl_4$ (Fisher Scientific/part of Thermo Fisher, Waltham, MA, USA, 98% purity). Thus, the aqueous suspensions (90 mL each) containing nanoparticles from the TS powder (540 mg each) and the aqueous solutions (90 mL each) containing the noble metals salts (26 mg of $AgNO_3$ and 32 mg of $KAuCl_4$) were mixed using a magnetic bar. The theoretical calculus predicted the 3 wt.% of the noble metals as a decoration element. Then, the reduction process was carried out using 10 mL of a 1.5 g/L aqueous solution of $NaBH_4$ (Aldrich, Sant Louis, MO, USA, 98% purity), which was dropped over the oxidic nanoparticle suspensions containing noble metal salts, followed by 24 h of evaporation and drying at 80 °C, see Figure 1.

The stoichiometry of the reduction reaction for Ag NPs synthesis can be summarized [19] as:

$$2{\cdot}AgNO_3 + 2{\cdot}NaBH_4 + 6{\cdot}H_2O \rightarrow 2{\cdot}Ag^0 + 7{\cdot}H_2 + 2{\cdot}B(OH)_3 + 2{\cdot}NaNO_3 \quad (1)$$

In a similar way, we propose the following chemical reaction for AuNPs generation:

$$2{\cdot}KAuCl_4 + NaBH_4 + 3{\cdot}H_2O \rightarrow 2{\cdot}Au^0 + H_2 + B(OH)_3 + NaCl + 2{\cdot}KCl + 5{\cdot}HCl \quad (2)$$

The samples obtained after the impregnation/reduction process were named TS_Au and TS_Ag and, together with the other two samples obtained after the pyrolysis process, TS and T, were studied from the point of view of photocatalytic, sensorial, and biocompatibility properties compared to a commercial standard sample—P25 Degussa.

2.2. *Morpho-Structural and Optical Characterization*

The elemental composition of the TiO_2-based nanopowders was estimated using Energy-dispersive X-ray spectroscopy (EDS), performed inside the Scanning Electron Microscope, FEI Co., model Quanta Inspect S, at 15 kV in high vacuum. The structural characteristics had been identified using a Bruker D8 diffractometer (Billerica, MA, USA), using Bragg–Brentano symmetry (Theta-Theta) and the copper anode. The Highscore Plus 4.8 software was used to handle data and calculate the powders' parameters. The Raman spectra were obtained using HORIBA LabRAM HR Evolution at room temperature. The excitation source was air-cooled He-Cd lasers, 325 nm/25 mW. Edge and bandpass filters were set at 325 nm for Raman measurements from 150 cm^{-1} to 4000 cm^{-1}, controlled using LabSpec 6 software, one column with the necessary motorized coupling optics for injecting the beam of an external UV laser in the instrument. The following parameters were used: 40X NUV objective, NA = 0.50, WD = 1 mm, 2400 g/mm holographic grating blazed at 330 nm (spectral range 190–650 nm) with pre-aligned holder, calibration, and tests. The structural investigations were carried out using the analytical electron microscope JEOL JEM ARM200F with an acceleration voltage of 200 kV, equipped with an EDX spectroscope JEOL JED-2300T (Akishima, Tokyo, Japan). The powders were grained and dispersed in ethanol. A drop of each solution was deposited on a Cu grid with carbon film and left to dry at room temperature. The specific surface area had been measured using BET Flowing Gas Surface Area Analyzers, Horiba SA-9600, with a 30% N_2 and 70% He gas mixture. For the X-ray photoelectron spectroscopy (XPS) investigation of all samples, ESCALAB Xi^+ (Thermo SCIENTIFIC Surface Analysis, Waltham, MA, USA) and Avantage software (version 5.978) were utilized. A spectrophotometer JASCO V-780 type, with an integration sphere (ISN-901i), was used for measuring the diffuse reflectance DR spectra of the samples (λ = 200–800 nm, scanning speed = 100 nm/min). Luminescence properties were investigated using HORIBA Fluorolog-3 equipment with a modified monochromator to iHR320. Powder had been irradiated using a xenon lamp with a wavelength of 260 nm, cut using a double-grating excitation monochromator. All measurements were performed at room temperature.

2.3. Sensor Tests

The sensors were tested in a system consisting of an amplifier (DHPVA-200 FEMTO, Messtechnik GmbH, Berlin, Germany) and a frequency counter (CNT-91 Pendulum, Spectracom Corp, Rochester, NY, USA), connected to a computer with Time View 3 software for different concentrations of methane (CH_4). Those different concentrations of CH_4 were obtained via homogenization with artificial air in different proportions. The nanoparticles used to obtain sensitive layers were homogenized in a solution of poly(ethyleneimine) (PEI) (Sigma Aldrich, St. Louis, MO, USA) and ethanol, at a concentration of 10 mg/mL. The concentration of the nanoparticle suspension in polymer solution was 8 mg/mL. The sensitive layers were deposited by spin coating, using a volume of 20 µL suspension for each deposition.

2.4. Photocatalytic Tests

The UV–Vis photocatalytic activities of the synthetized nanocomposite materials were determined using an etalon pollutant, i.e., methyl orange (MO), with initial concentration $C_{0,\,MO}$ = 130 µM. For UV measurements, a photoreactor integrating 6 × 6 W fluorescent lamps (λ_{max} = 365 nm, irradiation time ~2.5 h) was used. 170 mL of nanocomposite suspension, containing 1.0 g/L photocatalyst in etalon pollutant solution was evaluated. In order to keep the concentration of the dissolved oxygen constant throughout the whole experiment, the air was continuously purged. Using a JASCO V-780 spectrophotometer (Tokio, Japan), the decrease in MO concentration was monitored, by measuring the light intensity at λ = 500 nm. For Vis photocatalytic investigations, the MO concentration was evaluated at 495 nm using a JASCO V-780 spectrophotometer. By representing ln (C_0/C_t) vs. irradiation time (assuming first-order kinetics), where C_0 represents the MO concentration at the beginning of the experiment and the C_t is the MO concentration during the experiment, a linear regression was obtained. From the slope of the obtained curve, the photocatalytic rate constants were estimated.

The photocatalytic investigations′ evaluated error was determinate based on reproducibility tests and the obtained values were between 2 and 5%. Moreover, for all nanocomposites, the MO adsorption, in the working conditions, was negligible (lower than 4.5%).

2.5. In Vitro Cytotoxicity Assays

Human keratinocytes (HaCaT cell line from Cell Lines Services, Eppelheim, Germany) were seeded at a density of 6×10^4 cells/cm^2 in 96-well plates and 4×10^4 cells/cm^2 in T25 flasks in complete Dulbecco's Modified Eagle's Medium with 10% fetal bovine serum at 37 °C, in a humidified atmosphere with 5% CO_2. After the cells attached, these were incubated for 24 h with different concentrations (5, 25, 50, and 100 µg/mL) of nanoparticles. At the end of the incubation period, the cells were visualized using an Olympus IX71 inverted microscope (Olympus, Tokyo, Japan).

2.5.1. MTT Assay

The cell viability was determined with the 3-(4,5-dimethylthiazol-2-yl)-2,5-diphenyltetr azolium bromide (MTT, Sigma-Aldrich, St. Louis, MA, USA) assay, based on the succinate dehydrogenase mitochondrial activity in live cells. The culture medium was removed after 24 h and the cells were incubated with 1 mg/mL MTT solution for 2 h at 37 °C. Further, 2-propanol (Sigma-Aldrich, USA) was added to solubilize the formazan crystals and the absorbance was read at 595 nm, using the FlexStation 3 multi-mode microplate reader (Molecular Devices, San Jose, CA, USA).

2.5.2. Griess Assay

The concentration of nitric oxide (NO) in the culture medium, harvested after 24 h of incubation with nanoparticles, was measured with the Griess reagent. This is a stoichiometric solution (*v*/*v*) of 0.1% naphthyl ethylenediamine dihydrochloride and 1% sulphanilamide in 5% H_3PO_4. The mix obtained from equal volumes of culture medium and Griess reagent was subjected to an absorbance reading at 550 nm on a FlexStation 3 multi-mode microplate reader.

2.5.3. Lactate Dehydrogenase (LDH) Assay

The release of LDH in the culture media after 24 h of cell growth in the presence of nanoparticles was determined as an indicator of cell membrane damage using a commercial kit (Cytotoxicity Detection Kit^{PLUS} (LDH), Roche, Indianapolis, IN, USA). A volume of 50 µL of culture medium was mixed with a 50 µL mix of catalyst, according to manufacturer's instructions. After a 30 min incubation in the dark, the absorbance was read at 490 nm on the FlexStation 3 microplate reader.

2.5.4. Cell Lysis

HaCaT cells seeded in T25 flasks and incubated with 100 µg/mL nanoparticles were harvested after 24 h, washed with PBS, and lysed using sonication (3 rounds of 30 s) on ice with an ultrasonic processor (Hielscher UP50H, Teltow, Germany). The supernatant of cell lysate was collected after centrifugation at $10{,}000\times g$ for 10 min at 4 °C. The protein content was determined using the Bradford reagent and bovine serum albumin as standards.

2.5.5. Measurement of Glutathione (GSH) Content

GSH levels were determined using the Glutathione Assay Kit (Sigma-Aldrich, St. Louis, MO, USA). The cell lysate was first deproteinized (1:1, *v*/*v*) with the 5% 5-sulfosalicylic acid solution and centrifuged for 10 min at $5000\times g$ and 4 °C to remove the precipitated protein. A volume of 10 µL of supernatant was mixed with 150 µL of working mixture in a 96-well plate. The absorbances' recording was performed at 412 nm using the FlexStation 3 microtiter plate reader after 5 min of incubation at room temperature. The GSH concentrations were calculated based on a GSH calibration curve and were normalized to the protein concentration of cell lysates.

2.5.6. Advanced Oxidation Protein Products (AOPPs) Assay

Determination of the AOPPs level was carried out using a chloramine-T standard curve. A volume of 200 µL cell lysate was mixed with 10 µL of 1.16 M potassium iodide for

5 min at room temperature. Further, 20 µL of glacial acetic acid were added and the optical densities were read at 340 nm on the FlexStation 3 microtiter plate reader. The AOPPs level was normalized to the protein concentration of each sample.

2.5.7. Statistical Analysis

All in vitro data were analyzed using Student's *t*-test and illustrated using Microsoft Office Excel 2016. A value of p less than 0.05 was considered statistically significant.

3. Results

3.1. Structural Characterizations

3.1.1. EDS Analysis

EDS results, indicating a good correlation between precursor flows used in the LP process ($TiCl_4$, $SnCl_4$, synthetic air, and C_2H_4) and the composition expressed as atomic elemental concentrations in the obtained nanopowders (Ti, Sn, O, C, and Cl) are presented in Table 1. The TiO_2-based nanoparticles obtained in pyrolysis have a higher tin content (7.1 at.%) compared to our previous study (4.8 at.%) and were loaded with noble metal consisting of Ag—0.7 at.% and Au—0.2 at.%. Given these small values, 0.2 at.% for gold and 0.7 at.% for silver, each corresponding to 1.25 and 2.6 weight percent, respectively, and taking into account that 3 wt.% of the noble metals were initially added in both cases for decoration, it seems that part of the salts was either wasted on the vessel walls during the chemical reaction or did not react completely. It is also noticeable that the samples contain some impurities such as C, Cl, Na, and K, which are caused by precursors or reagents utilized in the synthesis processes, such as C_2H_4, $TiCl_4/SnCl_4$, $NaBH_4$, and $KAuCl_4$, respectively; the sample with the highest level of contamination is TS_Au (7.2 at.%), with all other samples showing significantly reduced contamination levels. Sample T contains weak traces of C (0.2 at.%) resulting from the decomposition of ethylene in the LP process. On the other hand, in the case of sample TS, this percentage of calcination-resistant C increases up to 2.1 at.%, together with the presence of traces of Cl (0.2 at.%). This is due to the formation of "butter of tin" in the LP process, which, by calcining the samples at 450 °C in air, evaporates or oxidizes, forming SnO_2. In the case of the TS_Au sample, the percentage of Cl increases up to 2.9 at.%, due to the gold precursor used for decoration ($KAuCl_4$), forming NaCl and KCl salts through the simultaneous use of $NaBH_4$ as a reducing agent in the CI process. In the case of the TS_Ag sample, the impurities are much smaller (<1 at.%) and are represented by traces of C and NaCl. The presence of these impurities is in good correlation with the XPS results presented below.

Table 1. EDS measurements, crystallographic parameters, band gap energy values and photodegradation efficiency for the TiO_2-SnO_2@NMs nanocomposite.

Samples			**P25**	**T**	**TS**	**TS_Au**	**TS_Ag**
EDS Results	Chemical composition [at.%]	NM	0	0	0	0.2	0.7
		Sn	0	0	7.1	6.0	5.8
		Ti	34.1	37.5	27.3	24.9	23.0
		O	65.9	62.3	63.3	61.7	69.6
	Chemical composition Impurities [at.%]	C	0	0.2	2.1	0	0.2
		Cl	0	0	0.2	2.9	0.1
		Na	0	0	0	3.8	0.6
		K	0	0	0	0.5	0
		Total	0	0.2	2.3	7.2	0.9

Table 1. *Cont.*

Samples			P25	T	TS	TS_Au	TS_Ag
XRD Results	Phase proportion [%]	A	89.7	62.8	37.0	34.6	36.9
		R	10.3	37.2	63.0	65.4	63.1
	Crystallite size [nm]	A	23.9	23.4	17.0	21.4	22.1
		R	37.3	27.3	14.2	13.0	24.3
Optical Results	Band gap energy [eV]	ΔE_g	3.2	3.05	3.04	3.06	2.73
	Fermi level	E_F-E_V	-	2.28	2.30	1.80	2.02
Photodegradation Results	Rate constant [10^{-3} min^{-1}]	UV	6.52	7.00	11.47	37.85	43.95
		Vis	0.25	0.29	0.28	9.11	18.52

3.1.2. XRD Analysis

The X-ray superposed diffraction patterns for the noble metal-free titania-based samples are presented in Figure 2. The comparison of the diffraction patterns between the commercial P25 Degussa (Evonik), obtained via combustion in the H_2-O_2 flame, and T, TS samples, synthesized using laser pyrolysis and calcined at 450 °C, are shown in Figure 2a; while the influence of the noble metals is presented in Figure 2b. All these samples contain the main titanium dioxide phases, Anatase and Rutile, corresponding to the ICDD database Powder Diffraction Files no. #01-070-7348 and #01-086-4329, respectively. The TiO_2 phase ratio has been calculated using the Spurr and Myers equation [20,21]. The TiO_2 samples have as predominant component, the Anatase phase, which shifts to the Rutile phase with the introduction of SnO_2 (Table 1).

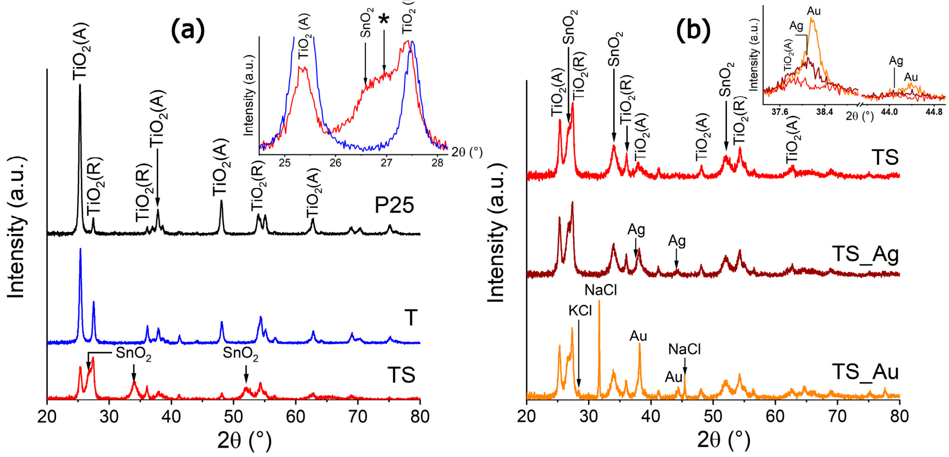

Figure 2. The X-ray diffractograms: (**a**) P25, T, and TS samples and (**b**) TS, TS_Au, and TS_Ag; (**a**) inset: magnification of the 2θ = 24–28° zone from T and TS powders diffractograms; (**b**) inset: magnifications of the 2θ zones between 37.3–38.8° and 43.6–45 from TS and noble metal-doped samples' diffractograms.

There is a broad and complex peak from 26° to 28° that consists of the (110) TiO_2 Rutile peak at 27.40° and the shoulder containing two nearby convoluted peaks at approximately 26.62° and 27.11°, belonging to the (110) reflection of the tetragonal SnO_2 phase (#01-071-5323) and, most probably, to a Ti-doped SnO_2 or a strained SnO_2 phase (noted with *), respectively (Figure 2a, inset).

The XRD peaks corresponding to the metallic Ag or Au were detected in the TS_Au/Ag samples (Figure 2b and its inset), corresponding to ICDD Files no. #03-065-2871 and #00-004-0784, respectively. The XRD lines of the gold metallic particles are more intense than that of the silver, at ~35 nm and ~17 nm, respectively. For the TS_Au sample, the small peak at 28.37° can be attributed to the (200) reflection of the KCl cubic phase (ICDD #04-00-9724), whereas the sharp peak positioned at 31.69° can be attributed to the (200) reflection of the NaCl cubic phase (ICDD #01-080-3939). Both those salts are byproducts of the gold salt reduction. The absence of residual salt XRD peaks in the TS_Ag sample can be explained by the rapid deposition of freshly seeded NPs upon reduction that allowed the elimination of the salt aqueous solution upon decantation. For the case of the TiO_2-SnO_2@Au NPs, the suspension was more stable and only the water was eliminated by evaporation, but not the alkaline salts.

The lattice parameters of the T sample are a = b = 3.7839 ± 0.0006 Å, c = 9.4935 ± 0.0035 Å for the Anatase phase; and a = b = 4.5762 ± 0.0064 Å, c = 2.9688 ± 0.0063 Å for the Rutile. The Cassiterite phase of the TS (and decorated samples) has a = b = 4.7263 ± 0.0138 Å and c = 3.1827 ± 0.0154 Å. These values are relatively close to the information contained in the ICDD database for these three phases. The introduction of the Sn precursor in the reaction also induces changes to the lattice parameters of the TiO_2 phases, whereby the Anatase phase has a = b = 3.8378 ± 0.0149 Å and c = 9.7757 ± 0.0386 Å, whereas the Rutile phase has a = b = 4.5959 ± 0.0179 Å and c = 2.9584 ± 0.0168 Å in the TS sample. The observed changes in the Rutile phase seem to be in the range of the calculus error (~0.02 Å for a and b, and ~0.01 Å for c), while in the case of the Anatase phase, the crystal structure is expanded in all directions by 0.0539 Å for a and b and by a much higher value of 0.2822 Å for the c lattice parameter. In our previous studies, we proved that synthesis variables like temperature, pressure, impurities, and increasing levels of doping have an impact on the conversion of the Anatase phase into the Rutile phase [18]. A possible explanation for the favoring of the Rutile phase formation in the presence of a tin precursor could be the faster formation of SnO_2 cassiterite nanoparticles in the laser oxidative pyrolysis flame than the TiO_2 ones, due to a lower metal–chlorine dissociation energy in the case of $SnCl_4$ versus $TiCl_4$ [22]. These SnO_2 NPs seeds can act as template for the condensation of the TiO_2 Rutile phase with a high crystalline similarity, while the lack of compatible nucleation centers will delay the Anatase phase condensation process, even if the Anatase phase formation is usually kinetically favored versus the Rutile phase.

Crystallite sizes were calculated using the Scherrer equation [23], averaging the values from the most intense peaks, and are listed in Table 1. The crystallite sizes of the TiO_2-SnO_2 samples are between 10 and 15 nm, meanwhile the Au NPs and the Ag NPs are between ~35 nm and ~17 nm, respectively.

3.1.3. Raman Analysis

Raman spectroscopy investigation uses inelastic photon scattering to determine vibrational modes, which are characteristic of the material. The Anatase bands in titania are usually positioned at 144 (E_g), 197 (E_g), 399 (B_{1g}), 515 (A_{1g}), 519 (B_{1g}), and 639 cm^{-1} (E_g) waveshifts, whereas those of the Rutile phase can normally be found at 143 (E_g), 235 (B_{1g}), 447 (E_g), and 612 cm^{-1} (A_{1g}) [24,25]. Unfortunately, the number of certain specific phonons can be drastically diminished due to the crystal's structure imperfections [26,27] and this can explain the absence of some Raman peaks in our samples. The Raman spectra of the P25, T, and TS samples presented in Figure 3 show peaks that could be attributed to the Anatase (148 cm^{-1}, 198 cm^{-1}, ~385 cm^{-1}, and ~505 cm^{-1}) or to the Rutile crystalline phase (250 cm^{-1} and ~615–618 cm^{-1}). All these peaks are shifted and, in the case of Anatase, this could be due to the background subtraction routine, while, for Rutile, this shift is significant and seems to be correlated with XRD data, where microstrains have been found. The broad low intensity peak at 765 cm^{-1} corresponds to the B_{2g} mode of the SnO_2 and is only observed for the TS and NM-decorated samples (Figure 3).

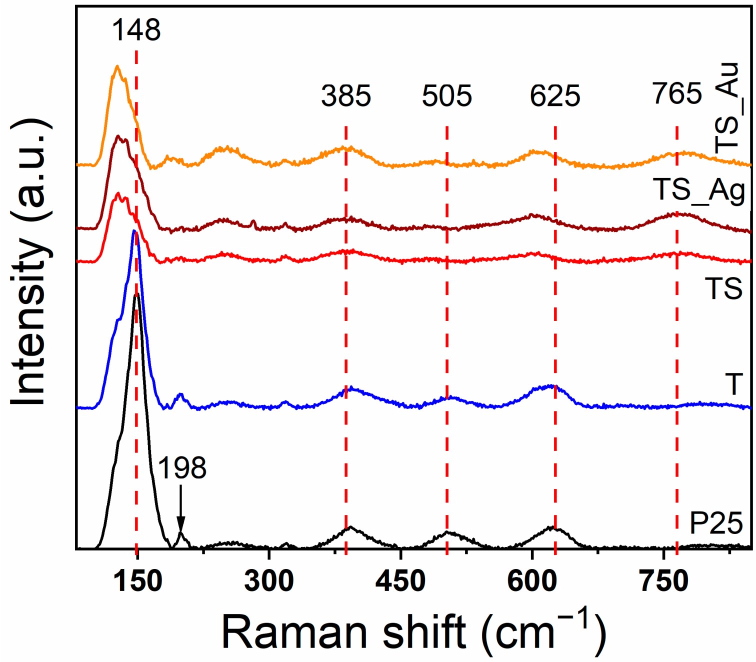

Figure 3. The Raman spectra of the pure TiO_2 powders, TiO_2 coupled with SnO_2 and TiO_2-SnO_2@NMs at room temperature, λ_{exc} = 325 nm.

The peaks begin to change their intensity and/or shift their position after decoration with NMs. For example, the peaks at ~505 cm^{-1} and 625 cm^{-1} decrease in intensity, but those at 250 cm^{-1} and 765 cm^{-1} increase. Also, when compared with the intensities of the TS Raman spectrum, those decorated with NMs show slightly higher intensities for all observed peaks. All these shifts are due to the modification of interatomic distances that change the normal vibrational modes and even create new ones, which are detected using Raman spectroscopy. These changes in crystal structure could be dislocations, point defects, or impurities [27]. There is also the possibility of point defects like oxygen vacancies appearing on the surface of the grain. In this case, any vibrations created in the grain's core begin to overlap with a new symmetry at the surface and diminish or amplify the energy for the new vibrational mode [26,27].

3.2. Morphological and Surface Area Characterization

3.2.1. TEM

The TEM/HRTEM images presented in Figure 4 provide information about the nanopowders corresponding to the TS_Au and TS_Ag samples, where relatively crowded, agglomerated/aggregated, and rounded nanoparticles can be observed in both samples (Figure 4a,b,e,f). The EDX spectra demonstrate the presence of noble metal nanoparticles and confirm the composition of the materials (Figure 4d,g). In the case of the TS_Au sample, with Au nanoparticles between 40 nm and 150 nm, TiO_2 nanoparticles betwen 10 and 60 nm in size were identified (Figure 4b,f). In the case of the TS_Ag sample, the TiO_2 nanoparticles mainly have sizes between 20 nm and 60 nm. According to the measurements in the HRTEM images, several phases of TiO_2 coexist, as follows: Anatase (tetragonal system, space group $I4_1/amd$ with lattice parameters a = 0.37922 nm and c = 0.95023 nm, with the plane family (101) at the interplanar distance of 0.35 nm) and the Rutile (tetragonal system, having the space group $P4_2/mnm$ with lattice parameters a = 0.453 nm and c = 0.2921 nm). In the HRTEM image presented in Figure 4c, it is possible to identify TiO_2 crystallites of the Rutile phase, with (110) plane families at 0.32 nm and a Ag nanoparticle showing the lattice fringes of the (200) planes of the Ag, with 0.2 nm spacing.

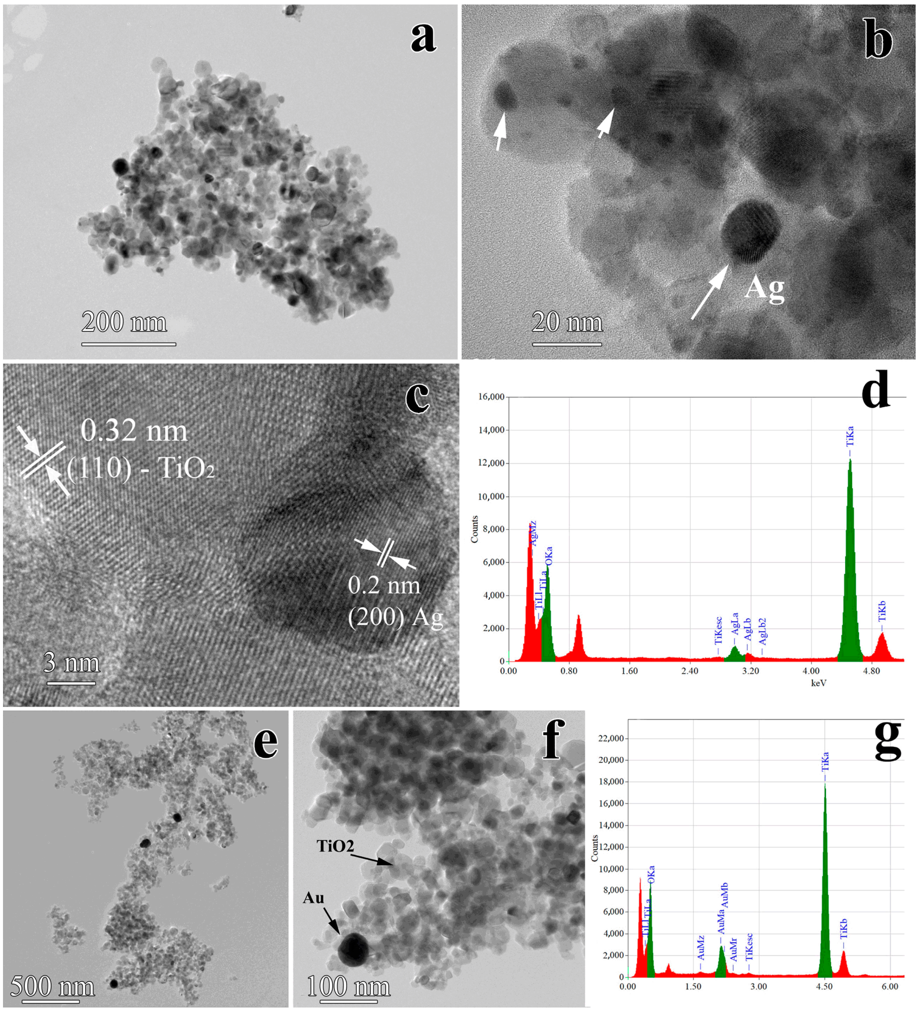

Figure 4. TEM/HRTEM images of the TiO_2-SnO_2 grain decorated with Ag (**a**–**c**) or Au (**e**,**f**) NPs. EDX spectra collected on oxidic particles aggregates containing Ag (**d**) or Au (**g**) NPs.

In the HRTEM image (Figure 4c), a Ag nanocrystallite connected with the TiO_2 Rutile phase is also presented. So, it is more likely that the Anatase phase is created at the beginning of the LP process and, as the temperature rises and grains form, the phase changes to Rutile at the boundary. By adding the $SnCl_4$ precursor to the synthesis process, the SnO_2 cassiterite seed particles are initially formed (due to the lower dissociation energy of $SnCl_4$ versus those of the $TiCl_4$ precursor [22,28]), having the same space group ($P4_2/mnm$) and tetragonal structure as the TiO_2 Rutile, thus inducing the crystallization of templated Rutile on their surfaces and, as a result, Rutile becomes the dominant phase over Anatase, which lacks the proper crystallization seeds. Moreover, the ionic radius of Sn^{4+} (83 pm) is only slightly greater than that of Ti^{4+} (74.5 pm) [29], so the strain induced by the Sn^{4+} ions substituting Ti^{4+} into titania crystallites is greater for Anatase than for Rutile, the latter phase having a very similar structure with cassiterite SnO_2; thus, the microstrain begins to appear in Anatase and not in Rutile. Regarding the Ag nanoparticles, they have sizes between 2 nm and 18 nm and are heterogeneously distributed among the TiO_2 nanoparticles (Figure 4a,b).

3.2.2. BET Analysis

Following the BET measurement, the specific surfaces corresponding to the studied samples were determined, resulting in the following values: 49.94 m^2/g, 52.59 m^2/g, 30.92 m^2/g, 21.73 m^2/g, and 31.20 m^2/g, which correspond to P25, T, TS, TS_Au, and TS_Ag samples, respectively. The addition of tin significantly decreased the surface in the case of the TS sample compared to the T sample, possibly due to the aggregation of the crystallites, as a result of the increase in the intrinsic density, since the SnO_2 density (6.95 g/cm^3) is higher than the TiO_2 density (4.23 g/cm^3). Another explanation is the coating of the porous nanoparticles with "butter of tin" ($SnCl_4 \cdot 5 \cdot H_2O$) and/or other tin tetrachloride hydrates formed in the vapor phase from undecomposed $SnCl_4$ molecules interacting with water vapors, provided by the incipient oxidation of the ethylene sensitizer, resulting in a much more hygroscopic raw nanopowder, compared to that obtained without tin. This led to the loss of micropore voids by sealing them with SnO_2 formed from those crystalohydrates, upon the post-synthesis calcination of nanopowders in air at 450 °C, leaving only large mesopore voids between the particles. Also, the presence of traces of C as well as NaCl and KCl impurities contribute to a decrease in the specific surface by embedding the nanoparticles in amorphous or crystalline layers, in the case of nanoparticles passed through the noble metal decorating process. Also, the lowest specific area measured for the TS_Au sample can be correlated with the high density of Au NPs (19.39 g/cm^3).

3.2.3. XPS Analysis

In order to determine the elemental composition, the chemical state, and the electronic state of the samples, XPS analysis was used and the results are shown in Figure 5. Obtained survey spectra of nanocomposites (TS, TS_Au, and TS_Ag samples) and synthesized TiO_2 (T sample) are shown in Figure 5a and indicate the presence of Ti, Sn, O, Au, and Ag, as well as C, Cl, K, and Na impurities. The C peak is mainly attributed to the adventitious carbon from the XPS instrument (the post-synthesis thermal treatment at 450 °C was carried out to remove unwanted carbon). From the high resolution XPS spectra of O1s (Figure 5b), all samples present three peaks at 529.9 eV, 530.6–531.3 eV, and 531.8–532.6 eV (see the inset), assigned to the lattice oxygen of metal oxides TiO_2/SnO_2 and non-lattice oxygen (from oxygen atoms close to oxygen vacancies or even from the strongly bonded OH, similar to those in hydroxides), as well as to surface-adsorbed H_2O or other weakly bonded oxygen-containing surface species. By superimposing the spectra, a substantial increase in the areas corresponding to non-lattice oxygen and to physiosorbed oxygenated species BE (binding energy) can be observed for the samples decorated with Au and Ag, this being an indication of oxygen vacancies, together with weakly absorbed water molecules on the TS_Au and TS_Ag samples' surface. This means that loading Au/Ag could cause the electrons to transfer at the interface of Au/Ag and TiO_2-SnO_2@NMs nanocomposites.

Further, in Figure 5c,d, the high-resolved XPS spectra of Ti 2p and Sn 3d are acquired in both TS composites. As can be seen, the spectra of the samples decorated with Au or Ag are shifted and/or show larger BE values compared to the TS sample, both for Ti 2p and for Sn 3d. Such BE changes have been reported in the literature for TiO_2 and SnO_2 systems decorated with Au or Ag [30,31] and probably result from interactions between metals and TiO_2-SnO_2 nanocomposites. The inset in (c) shows that, in the TiO_2 sample with Sn content (TS sample), the XPS spectrum of Ti 2p is identical to that of the control sample (T sample). Moreover, Figure 5e,f show the high-resolution XPS spectra of Au 4f and Ag 3d in the TS_Au and TS_Ag samples, respectively. The Au $4f_{5/2}$ and Au $4f_{7/2}$ spin-orbital splitting photoelectrons were located at 86.47 eV and 82.80 eV (ΔE = 3.67 eV), indicating that Au nanoparticles are almost reduced to metallic Au^0. Usually, the bulk metallic Au $4f_{7/2}$ spin-orbital splitting photoelectron is located at BE = 84 eV. The shift of the binding energy towards lower values may be ascribed to the electron transfer from oxide support to the Au nanoparticles [32]. The results presented in Figure 5f, in which the peaks located at 373.2 eV and 367.2 eV are assigned to metallic Ag $3d_{3/2}$ and Ag $3d_{5/2}$, respectively, indicating that Ag exists only as metallic Ag^0 in the TS_Ag sample (no oxidation), are also in accordance with the previous results. Compared with bulk metallic Ag, where BE = 368.2 eV for Ag $3d_{5/2}$ [33] the binding energy also has a negative shift.

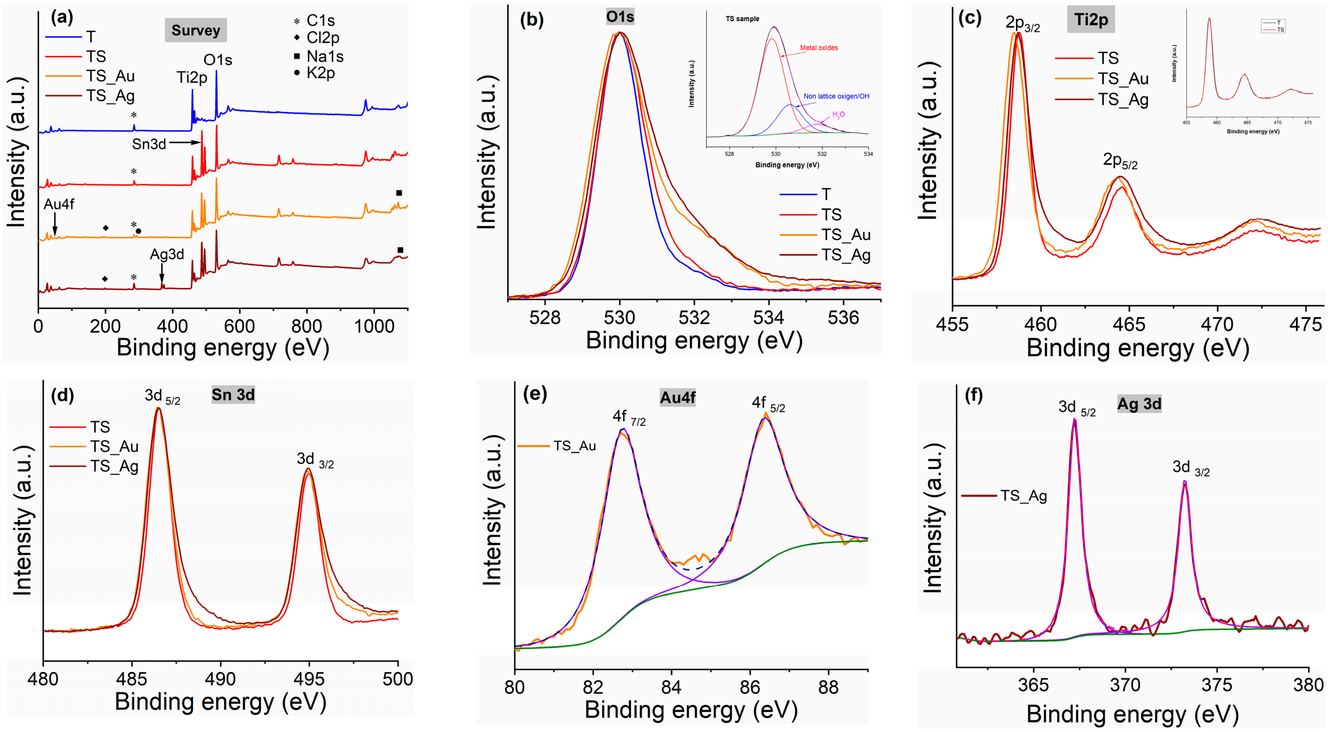

Figure 5. XPS spectra of T, TS, TS_Au, and TS_Ag samples: (**a**) survey spectra; (**b**–**f**) high-resolution XPS spectra of (**b**) O 1s, (**c**) Ti 2p, (**d**) Sn 3d, (**e**) Au 4f, and (**f**) Ag 3d core lines. The inset in (**b**) deconvolves and identifies the peaks that contribute to the XPS spectra of the O1s core level obtained for the TS sample (**c**) compared to the Ti 2p XPS spectra of the T and TS samples.

3.3. Optical Characterizations

3.3.1. UV/Vis Diffuse Reflectance Spectroscopy

The optical properties of the titania-based nanocomposites, obtained using LP followed by CI, as compared with the commercial Degussa P25 sample, were investigated using UV–Vis diffuse reflectance spectroscopy. Figure 6a shows the DRS-UV/Vis absorption spectra of the investigated samples. The recorded spectra of Au- and Ag-decorated samples demonstrate an important enhanced absorption in the visible range (450–600 nm), owing to the surface plasmon resonance effect induced by metal nanoparticles (gold and silver) from the titania matrix [34]. The absorbance in the visible region indicates that lower energy transitions are possible for the metal NP matrix. The enhanced light absorption can, therefore, provide more photocharges, needed for photocatalytic applications. From the reflectance [F(R)] spectra and using the Kubelka–Munk (K-M) formalism and the Tauc plot [17,35,36], the band gap energy values, E_g, were estimated. The E_g values (direct transition type) for all studied samples are summarized in Table 1 and illustrated in Figure 6b for the TS_Ag sample.

For the undecorated samples, the analysis shows that the band gap energy value series is $E_{g\ P25} > E_{g\ T} > E_{g\ TS}$. Interestingly, upon decoration with Ag, the TS matrix demonstrates a significant decrease in the E_g value (Table 1). Contrarily, the Au-decorated TS matrix lead to an insignificant increase in E_g value. Thus, the further the photocatalytic activity measurements are encouraged by the previously results [17], which proved that by the narrowing of the metal-loaded TiO_2 samples band gap, this leads to an increase in the photocatalytic activity to the visible range. Moreover, these results could be the effect of the corroborated influence of (i) the specific mixture of the Anatase and Rutile phases, (ii) the presence of metal doping, (iii) the nanoparticle size of both the TiO_2 and metal (Au and Ag) particles, and (iv) the residual carbon.

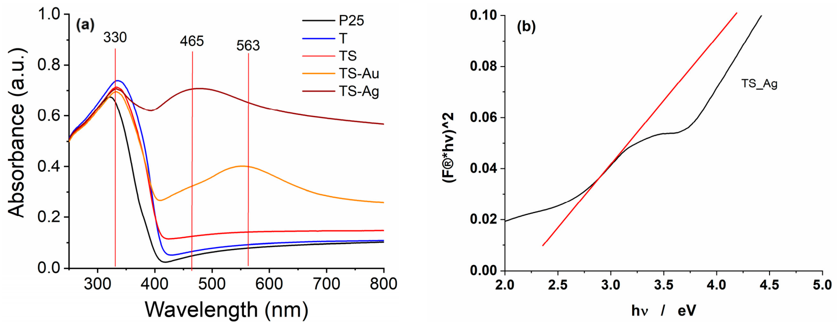

Figure 6. UV–Vis absorption spectra for P25, T, TS, TS_Au, and TS_Ag samples (**a**) and Kubelka–Munk transformation of reflectance spectra, regarding bandgap value of the TS_Ag sample (**b**).

3.3.2. Photoluminescence

The luminescence of the TiO_2 samples decorated with NMs is presented with the big and wide PL band (Figure 7). We should mention that the second harmonic from the light source is present in the spectra (λexc = 260 nm). Detected wide PL bands are complex and there are several peaks and inflections that could be observed.

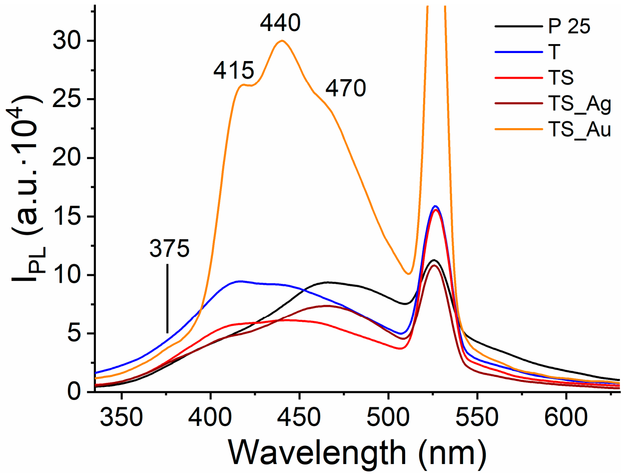

Figure 7. Photoluminescence spectra of the TiO_2 powders coupled with SnO_2 and decorated with NM at room temperature, λ_{exc} = 260 nm.

First, the PL properties begin to be visible from the UV region (350 nm). The first band is seen at around 375 nm (3.30 eV), which corresponds to the band-to-band transitions, is most probably connected to the excitonic annihilation [37]. This band is present in all samples and has around the same intensity. The next three PL bands are at 415 nm (2.99 eV), 440 nm (2.82 eV), and 470 nm (2.64 eV). As it was shown previously, the TiO_2 powder has Anatase and Rutile phase and the band gaps are indirect (3.20 eV) and direct (3.00 eV), respectively [9,37–39]. The band at 415 nm could represent the direct transition from the Rutile phase or an excitonic annihilation. At the same time, the high intensity relative to the 375 nm band could be a result of the self-absorption of light from the depth of the grain (Anatase phase) by the surface (Rutile) and photon reemission. At the surface of the grain, some point defects could also be formed due to the residual impurities or vacancies, for example, oxygen vacancies, creating a donor level in the band gap [40]. These imperfections work in the same way as Rutile phase, re-emitting the light with less energy at the 470 nm PL band. Donor levels remain with the hole after radiation (or self-absorption) and the excited electron is connected to the hole, forming a trapped exciton. The binding energies of trapped excitons are several meV less than free excitons and, in our case, the 440 nm band is 17 meV less than Rutile direct band gap.

The PL intensities of all samples are relatively equal, represented by one of the dominant bands. For example, sample T has a dominant 415 nm band, while P25 and TS_Ag samples have a band at 470 nm. But there is an exception, the TS_Au sample, which has a band intensity three times higher than others. The cause of that behavior is the presence of the NaCl and KCl impurities, found in the EDS, XRD, and XPS results. The TEM analysis points towards the formation of big Au particles on the surface of the TiO_2/SnO_2 powder that can cause the attraction of the electrons to the metal particles and produce a higher yield of the recombination process in its vicinity.

The binding energy of the electron in the valance band could be excited and analyzed using the XPS method (Figure 8). This technique is usually used to determine the elemental composition at the surface of the sample. At the same time, the first observed band in the XPS spectra could give us information about the Fermi level, because electrons obey the Fermi–Dirac distribution [41].

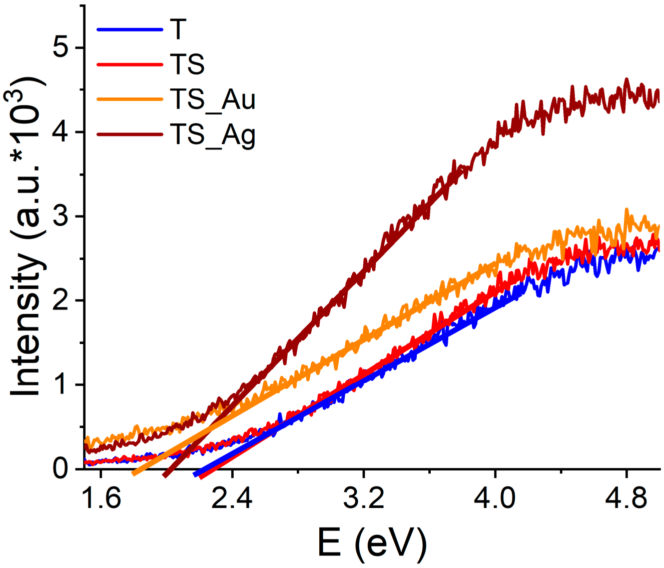

Figure 8. The Fermi level calculation from XPS spectra.

As a result, the extrapolation of the tangent line to the x-axis of the first band shows us the energy distance between the Fermi level and the valance band. This technique gives us the following numbers: 2.28 eV (T sample), 2.30 eV (TS sample), 2.02 eV (TS_Ag), and 1.80 eV (TS_Au sample). The band gap obtained from the Tauc Plot has a calculus between 2.73 eV and 3.05 eV (Table 1) and it is obvious that the Fermi level is shifted to the conduction band, demonstrating that all samples are n-type and the free charge carriers are electrons. The Fermi level shifts to one of the bands when there are supplementary donor or acceptor levels in the band gap. This shift is more pronounced when the concentration of these levels increases. Looking at the obtained numbers, there is a trend that the NMs increase the number of electrons in the conduction band and fills the traps formed by the donor levels. The TS_Au sample has the most significant shift of Fermi level, promoting the increase in the PL bands' intensities. Also, these shifts of Fermi level will increase the rate constant of the photoactivity over methyl orange.

4. Applications in the Environmental

4.1. Photocatalyst—Cleaning up Hazardous Substances

In order to prove the obtained samples' (T, TS, TS_Au, and TS_Ag) photoactivity effect on the hazardous substance in water, a standard compound (methyl orange, MO), used in photodegradation or photocatalytic discoloration investigations [17,18], was chosen. The MO (an anionic azo dye) photodegradation was evidenced for all samples, under both ultraviolet and visible light (Figure 9).

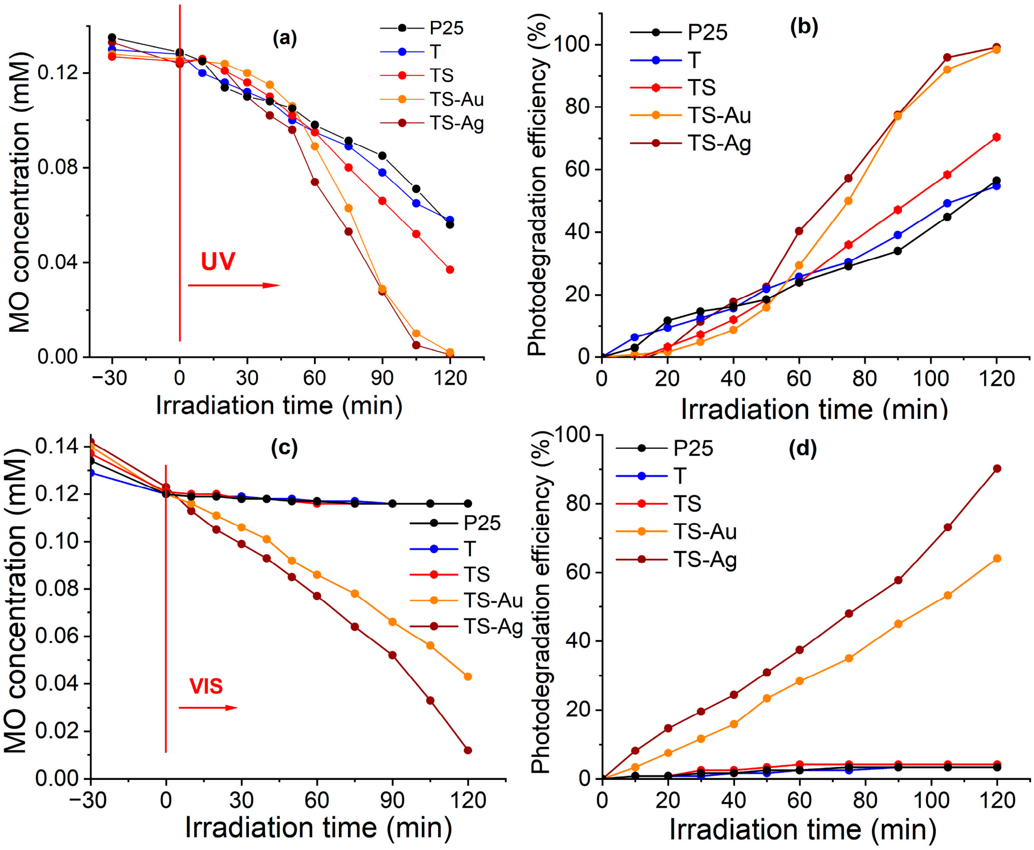

Figure 9. Adsorption and photocatalytic degradation profiles of MO during UV (**a**) and Vis (**c**) irradiation, using the indicated samples, and the corresponding MO photodegradation efficiency in time under UV (**b**) and Vis (**d**) irradiation.

At the beginning of each experiment, the equilibrium of the MO adsorption process on the nanocomposite surface was achieved by keeping the photocatalyst aqueous suspensions in the presence of MO in the dark (for a duration of 30 min). The MO photodegradation (with decreasing concentration) on our suspended photoactive samples versus UV or Vis irradiation time is presented in Figure 9a,c, respectively. As can be seen in Figure 9a, for all the titania-based samples, an ultraviolet-enhanced photoactivity against the MO was obtained (Figure 9a). It is worth noting that, in the first 60 min of UV irradiation, the TS_Ag nanocomposite demonstrated the best photoactivity among all the prepared photocatalysts and this behavior is maintained to the end of the photoactivity experiment. It is interesting to see that at the end of the UV irradiation process, the TS_Au photocatalyst shows similar photoactivity. The corresponding photodegradation efficiency vs. UV irradiation time for all obtained samples is presented in Figure 9b and the obtained MO photodegradation rate constant, k, is presented in Table 1. It must be emphasized that the rate constant value for the TS_Ag nanocomposite photocatalyst is ~7 times higher than that obtained for the unmodified P25 photocatalyst. Moreover, the activity of the TS_Ag photocatalyst is comparable, under UV or Vis irradiation, and the comparison trend for the photodegradation process is evidenced in Figure 9a,c.

Under Vis irradiation (Figure 9c,d), MO decomposition and photodegradation efficiency curves are more separated, in comparison to those recorded under UV irradiation (Figure 9a,b). It is clear that the metal nanoparticle containing TiO_2-SnO_2@NMs samples reveals considerably higher rate constants (~75 times) in comparison to TS, T, or P25 photocatalysts (Table 1). Moreover, the metal type (Au or Ag) present in the TS matrix considerably influences the photocatalytic activity under Vis irradiation. Thus, a significantly diminution of the MO amount, which means a considerably rise in the degradation process, is obtained for the TS_Ag nanocomposite, in comparison with all other prepared photocatalysts (Figure 9c). Thus, for bare TS, T, and P25 samples, there is no visible absorption (Figure 9c), which means that they exhibit no MO photodegradation activity (Table 1). The decreasing MO concentration on the surface of the nanocomposites under Vis light can be explained by the electron transfer from the metal NPs to the conduction band of the semiconductor. This behavior is explained via the surface plasmon resonance effect of Au and Ag nanoparticles decorating the TS surface. A comparable explanation was given in [17], where the presence of Pt, Au, and Ag nanoparticles on the TiO_2 surface was studied.

The highest photocatalytic performance of the TS_Ag nanocomposite may be due to its high exciton lifetime [17], which can be clarified by the approaching of the Fermi level to the conduction band of the semiconductor. Consequently, a rapid electron transfer between Ag and the oxide matrix is assured, leading to the production of very reactive superoxide and hydroxyl radicals, which, in turn, enhance the photocatalytic activity of the TS_Ag nanocomposite [17,42]. Moreover, the high photocatalytic activity induced by the Ag nanoparticle-decorated matrix, in comparison to the other metal nanoparticle-decorated semiconductor matrices, was explained by Kaur et al., based on the high conductivity and low work function of Ag [43], as well as being evidenced by Scarisoreanu et al. [17].

The decreased charge carrier recombination [44] and fast photodegradation of MO under UV irradiation, on the TS_Au and TS_Ag nanocomposites, compared to bare TS, T, and P25 (Figure 9a) is as a result of the increase in exciton lifetime in the metal-decorated nanocomposite matrix. This behavior can be associated with the formation of the Schottky barrier between Au or Ag nanoparticles and the semiconductor matrix.

The photocatalytic decomposition of MO with $c_0 = 130\ \mu M$ under UV irradiation on the TS_Ag nanocomposites leads to a rate constant value of $43.95 \times 10^{-3}\ min^{-1}$, while the equivalent rate recorded under Vis irradiation was lower, at $18.52 \times 10^{-3}\ min^{-1}$ (Table 1). There are many reports in the literature where the researchers combine the synergetic effects of TiO_2 and SnO_2 in order to increase their photodegradation performance on toxic contaminants in aqueous media [12,18,45,46]. Moreover, the metal nanoparticle's presence on the semiconductor matrix provides a better tunability for visible absorption [46], stops the recombination of e^-/h^+ pairs, and enhances e^-/h^+ separation, leading to an improvement in the photocatalytic performance. Compared to the results published in our previous studies, an increase in photodegradation efficiency was achieved. For TiO_2-SnO_2 nanocomposites, the photodegradation efficiency in UV light was $9.16 \times 10^{-3}\ min^{-1}$, while, in the case of simple TiO_2 nanoparticles decorated with Ag, the photodegradation efficiency in Vis light was $16.78 \times 10^{-3}\ min^{-1}$, both values being lower when compared to the results obtained in this study [17,18]. Thus, the improved photocatalytic effect of the obtained TiO_2-SnO_2@NMs nanocomposites is a result of the effects of different parameters, such as the TiO_2 and SnO_2 nanocomposite matrix, the presence of metal nanoparticles on the semiconductor surface, the nanocomposite preparation technique, the crystalline phase proportion in semiconductor matrix, the amount of NMs, the size and dispersion on the nanocomposite surface, and the nanocomposite active surface area.

The performant photodegradation of MO in the presence of our TiO_2-SnO_2@NMs nanocomposite can be extrapolated for the photodecomposition of other structurally related anionic azo dyes/pollutants, such as Acid Orange 7, Acid Red 88, Congo Red, Methyl Red, etc. Due to the photodegradation mechanism, based on the photogeneration of reactive oxygen species [47], we can also extrapolate that our NM-decorated nanocomposites may be used for catalytic degradation under UV/VIS light for other organic water-soluble pollutants (such as drugs, pesticides). Moreover, even if the TiO_2-SnO_2@NMs nanocomposites' production cost is higher than that of pure titania, they have the advantage of being active under visible light (pure TiO_2 only acts under UV light), which can be easily provided by solar radiation. Noticeably, under UV lamp irradiation, those NM-decorated nanocomposites show higher effectiveness in dye photodegradation when compared to pure TiO_2 or TiO_2-SnO_2 and also with reference to the commercial Degussa P25 nanopowder.

4.2. Sensors for Environmental Stages

The nanoparticles chosen to obtain sensitive layers for SAW sensors were T, TS, TS_Ag, and TS_Au and the sensors obtained based on these nanoparticles were renamed S1/T, S2/TS, S3/TS_Ag, S4/TS_Au, and S5/Polymer, respectively. Without exception, these sensors responded to all CH_4 concentrations tested (from 0.02 to 0.1% methane in air) and their frequency shifts can be seen in the graph in Figure 10. As the gas concentration increases, the frequency shift also increases for all sensors.

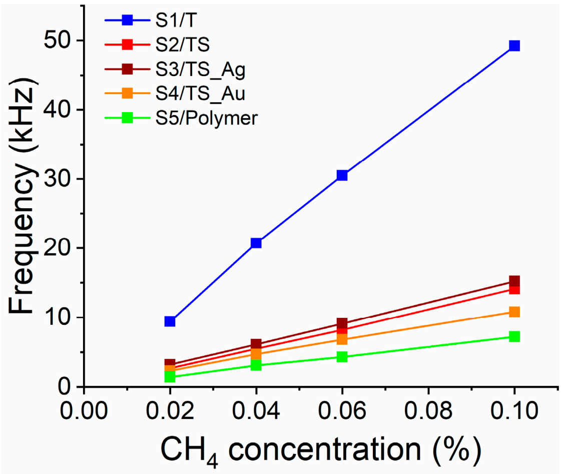

Figure 10. The frequency of the sensors at different concentrations of CH_4.

In the case of the S1/T sensor, a sharp difference in the frequency shift is noticeable, when compared to the other studied sensors. Taking into account that both TiO_2 and SnO_2 are semiconductor oxides with a sensitivity for CH_4 [4,5], we can appreciate that its results are based on the larger specific surface area of TiO_2 nanoparticles from the sensitive layer of the S1/T sensor, as can be seen from Table 1. Thus, the specific surface area of the sensitive material has a very important role for the development of sensors with the highest sensitivities. Also, the S5/Polymer sensor, which had only polymer in its sensitive layer, recorded the lowest frequency values, which confirms the contribution of the nanoparticles in improving the sensitivities of the sensors.

Based on structural similarity, the results obtained for methane detection using our TiO_2-based NPs/PEI nanocomposite in SAW sensor, we can expect this sensor to also be responsive to other light-saturated hydrocarbons such as ethane, propane, or butane, including LPG vapors (Liquefied Petroleum Gas). In comparison to the current state of technology, in terms of gas detection, the commercial sensors for reductive gases, such as methane, are usually conductometric-type, based on tin dioxide, which requires heating at a few hundred °C for gas detection. SAW sensors work at room temperature and benefit from the high specific surface of the oxidic NPs incorporated in the polymeric layer. They have low power consumption, fast responses, a good sensing effectiveness at low gas concentration, can be tuned to enhance selectivity, and are easy to implement, due to the facile deposition of polymer-NPs' sensitive layer via spin-coating.

4.3. Toxicity of Nanoparticles

The results obtained from the MTT assay (Figure 11a) revealed a concentration-dependent decrease only for the incubation with the P25 sample.

Also, a slight decrease, by 10%, from control was observed for the T nanoparticles. For the other samples tested, the levels were almost similar to those of control, confirming their low cytotoxicity.

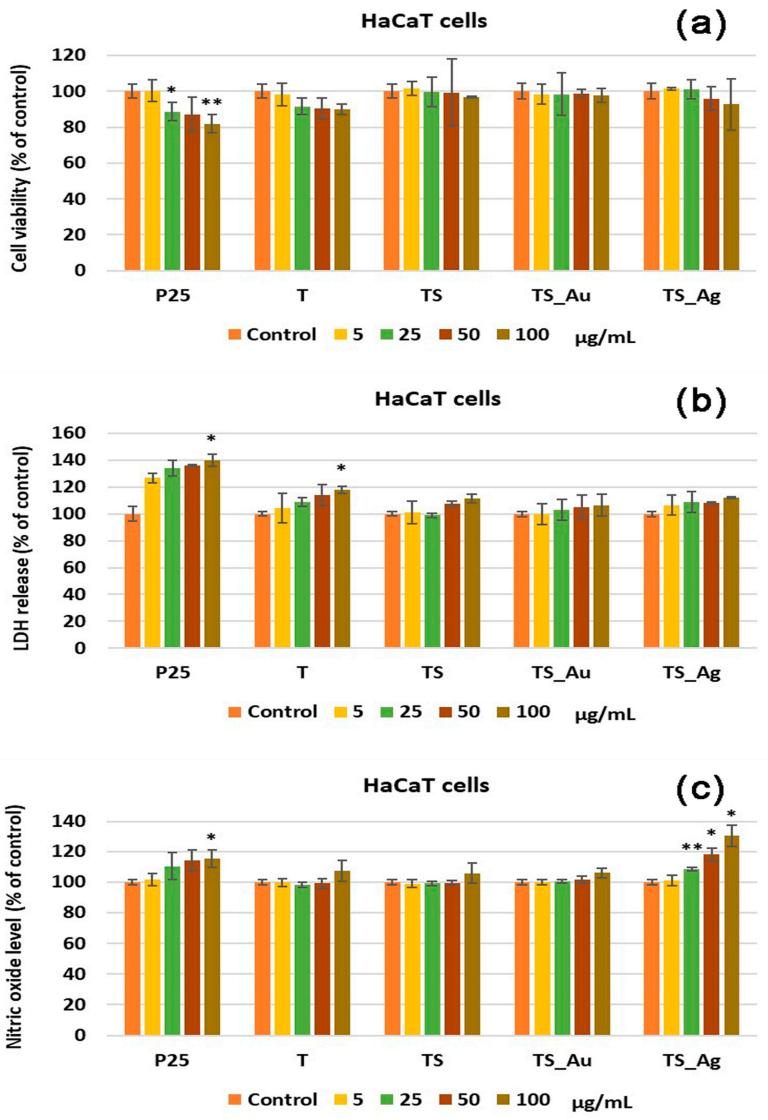

Figure 11. Cell viability (**a**), lactate dehydrogenase (LDH) release (**b**) and nitric oxide level (**c**) were measured after 24 h incubation of human keratinocytes HaCaT with different concentrations of nanoparticles (5, 25, 50, and 100 µg/mL). Results are calculated as mean ± SD (n = 3) and presented relative to control cells. * $p < 0.05$ and ** $p < 0.01$ compared to control.

Furthermore, the evaluation of LDH release (Figure 11b), which serves as an indicator of cell membrane integrity, showed that P25 induced the loss of cell membrane integrity, as the values increased up to 140% compared to the control for the highest concentration tested. This suggests that exposure to P25 nanoparticles resulted in cellular damage, leading to the leakage of LDH from the cells, correlating with the cell viability decrease. Additionally, a slight increase (around 120% compared to the control) in LDH release was observed for the highest concentration of the T sample, indicating a potential adverse effect on cell membrane integrity for this sample, in big quantities.

Regarding the NO levels shown in Figure 11c, the results revealed a concentration-dependent increase for both P25 and TS_Ag nanoparticles, suggesting that these particles could induce NO production. Increased NO levels are related to cytotoxic effects, because this molecule is synthesized and released in inflammation, oxidative stress, and apoptosis. However, the other samples, T, TS, and TS_Au, did not significantly modify the NO levels compared to the control, being in agreement with unchanged cell viability.

In order to further explore the effect of these nanoparticles on human keratinocytes, we selected only the highest concentration, 100 µg/mL.

First of all, the cell morphology after 24 h of incubation (Figure 12a) revealed a full coverage of the flask's surface for all nanoparticles tested, except the case of P25, which exhibited more floating cells compared to the other samples, confirming the decrease in cell viability, as was measured using the MTT assay. In addition, to evaluate the oxidative stress, two parameters, protein oxidation and reduced glutathione, were measured (Figure 12b). There was a significant increase in AOPPs level ($p < 0.05$) after the incubation with P25 compared to the control, confirming the potential of these nanoparticles to generate free radicals that oxidize proteins, altering their function and cell metabolism. This result for P25 also correlated with the slightly decrease in GSH content, indicating a perturbation of redox homeostasis and the initiation of oxidative stress. In contrast, the other types of nanoparticles did not significantly modify the AOPPs level compared to the control. Regarding the GSH content, only the TS_Ag sample induces a slight increase compared to the control and this could be related to the elevated NO release.

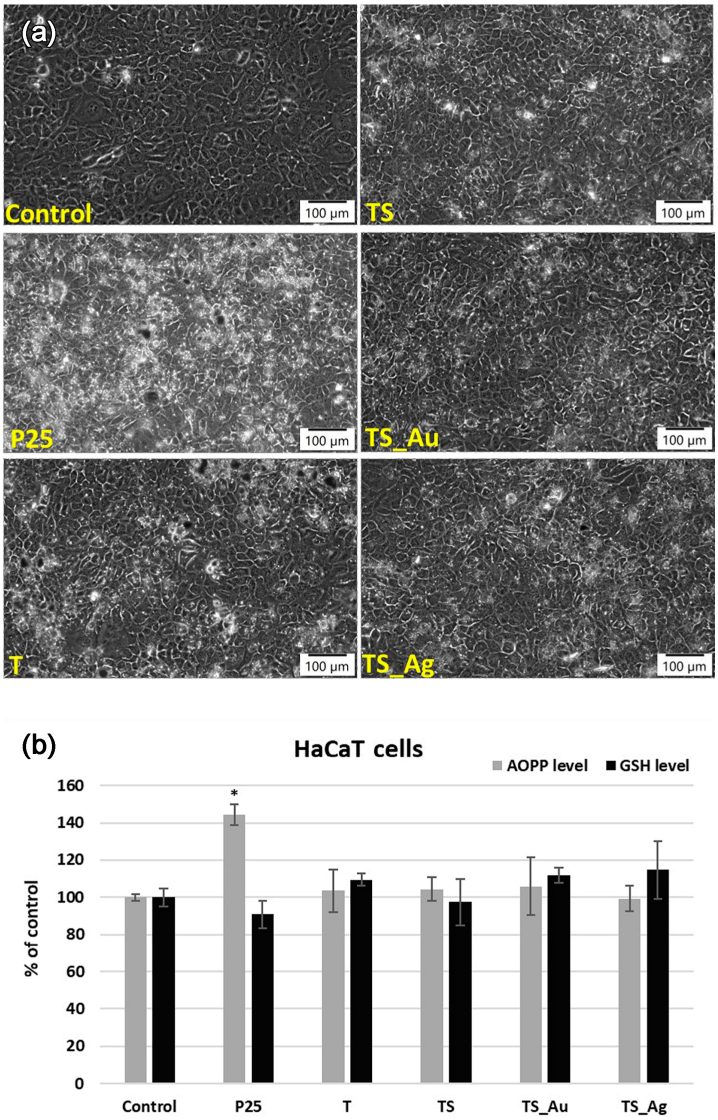

Figure 12. (**a**) Phase contrast images of human keratinocytes, HaCaT, incubated for 24 h with 100 µg/mL nanoparticles and (**b**) levels of advanced oxidation protein products (AOPPs) and reduced glutathione (GSH) in these cells. Results are calculated as mean ± SD (n = 3) and presented relative to control cells. * $p < 0.05$ compared to control.

Taking into account the fields of use of TiO_2-SnO_2-based nanomaterials (cosmetics, sunscreens, food packaging, and biomedical devices), the unveiling of the biocompatibility properties of the samples is of paramount importance. Our in vitro results showed a good biocompatibility of TiO_2-SnO_2@NMs compared to the high toxicity of bare TiO_2, being in alignment with the current European standards and regulations focused on human health and environmental safety implications of manufactured nanomaterials [48]. By demonstrating compliance with the European Chemicals Agency's (ECHA) guidelines and the Registration, Evaluation, Authorization, and Restriction of Chemicals' (REACH) requirements, our nanomaterials could be safely and successfully integrated into diverse applications.

5. Conclusions

Efforts towards sustainable and responsible technological advancements have led to the efficient enhancement of titania's surface with tin oxide and noble metals (Au/Ag), through LP and CI methods. The introduction of Sn (7%) in TiO_2 samples leads to the increased proportion of the rutile phase (from 37.2% to 63.0%), together with the decrease in the mean crystallite dimensions (from 27.3 nm to 14.2 nm). The addition of noble metals, Au—0.2 at.% and Ag—0.7 at.%, to these nanoparticles has induced a slight reduction in the specific surface area of the samples to 21.73 m^2/g and 31.20 m^2/g, respectively, as compared to the pure TiO_2 sample—52.59 m^2/g. The TEM analysis for the samples reveals that TiO_2-based nanoparticles with dimensions between 10 and 60 nm, loaded with gold and silver nanoparticles (2–18 nm), have been obtained. The optical characterizations of TiO_2-SnO_2@NMs nanopowders demonstrate an improved absorption in the visible spectrum, due to the effect of surface plasmons; the presence of Ag^0 and Au^0 metallic nanoparticles on the TiO_2 surface was also certified using XPS analysis. Comprehensive morpho-structural and optical characterizations have set the stage for evaluating the environmental and biomedical applications of these nanocomposites' applications. The synthesized TiO_2-SnO_2@NMs showcased remarkable multifunctionality features. As gas sensors for CH_4 detection, all nanocomposites exhibited a responsive behavior across various concentrations, with the S1/T sensor standing out due to its larger specific surface area. The integration of nanoparticles in the sensitive layer significantly improved sensor sensitivities, contributing to sustainable and efficient gas sensing technologies. As photocatalysts, these nanocomposites demonstrated an enhanced sustainability by outperforming TiO_2 P25 in degrading MO pollutants under both UV and visible light. The creation of TiO_2-SnO_2 nanocomposites augmented photocatalytic efficiency and their decoration with noble metals, particularly Ag, further increased photodegradation efficiency under visible light. The photodegradation efficiency has been amplified 6 or 7 times under UV radiation and by 30 or 60 times under visible light radiation, by decorating TiO_2-SnO_2 with Au and Ag, respectively. This sustainable approach facilitates a more efficient electron transport to the surface, highlighting the potential of these nanocomposites in advancing eco-friendly photocatalytic applications. Moreover, the biocompatibility assessments revealed that TiO_2-SnO_2-based nanoparticles exhibit a higher compatibility with skin cells, compared to conventional TiO_2 P25 and TiO_2 nanoparticles obtained using pyrolysis. These findings underscore the importance of exploring alternative nanoparticle compositions and sustainable synthesis methods, aligning with the broader goals of environmental and human safety. In conclusion, the emphasis on sustainability in these nanocomposites, particularly in enhancing sensory and photocatalytic features and promoting higher biocompatibility, marks a significant stride towards responsible technological advancements for a greener and safer future.

Author Contributions: E.G.: Conceptualization, Methodology, Writing—review and editing; M.S.: Conceptualization, Methodology, Writing—review and editing, Supervision; C.F.: Methodology, Investigation; E.D.: Formal analysis, Investigation; A.C.: Formal analysis, Investigation; I.P.M.: Conceptualization, Investigation, Writing—review and editing; C.V.: Formal analysis, Investigation; A.C.G.: Formal analysis, Investigation; A.V.M.: Formal analysis, Investigation; C.I.F.: Investigation, Writing—review and editing; M.S.S.: Investigation, Writing—review and editing. All authors have read and agreed to the published version of the manuscript.

Funding: This research was supported (or financed) by the Romanian Ministry of Research, Innovation and Digitalization under Romanian National Core Program LAPLAS VII—contract no. 30N/2023 and CNCS-UEFISCDI, contract number 31TE/2022 Project. NIMP authors acknowledge funding from the Romanian Ministry of Research, Innovation and Digitization through the Core project PC3-PN23080303.

Institutional Review Board Statement: Not applicable.

Informed Consent Statement: Not applicable.

Data Availability Statement: No new data were created or analyzed in this study. Data sharing is not applicable to this article.

Conflicts of Interest: The authors declare no conflicts of interest.

References

1. Zhang, Y.; Cao, M.; Li, R.; Chen, X.; Dong, H.; Liu, X. Explosive Characteristics and Kinetic Mechanism of Methane–Air Mixtures under High-Temperature Conditions. *ACS Omega* **2023**, *8*, 4251–4260. [CrossRef] [PubMed]
2. Li, J.-J.; Qi, X.; Xie, F.; Wu, D.; Fan, Z.-Q.; Cui, X.-Q. Methane gas adsorption and detection using the metal-decorated blue phosphorene. *Appl. Surf. Sci.* **2022**, *596*, 153511. [CrossRef]
3. Wang, C.; Yin, L.; Zhang, L.; Xiang, D.; Gao, R. Metal Oxide Gas Sensors: Sensitivity and Influencing Factors. *Sensors* **2010**, *10*, 2088–2106. [CrossRef]
4. Fujishima, A.; Honda, K. Electrochemical Photolysis of Water at a Semiconductor Electrode. *Nature* **1972**, *238*, 37–38. [CrossRef] [PubMed]
5. Comert, B.; Akin, N.; Donmez, M.; Saglam, S.; Ozcelik, S. Titanium Dioxide Thin Films as Methane Gas Sensors. *IEEE Sens. J.* **2016**, *16*, 8890–8896. [CrossRef]
6. Yang, B.; Zhang, Z.; Tian, C.; Yuan, W.; Hua, Z.; Fan, S.; Wu, Y.; Tian, X. Selective detection of methane by HZSM-5 zeolite/Pd-SnO_2 gas sensors. *Sens. Actuators B Chem.* **2020**, *321*, 128567. [CrossRef]
7. Mandal, D.; Banerjee, S. Surface Acoustic Wave (SAW) Sensors: Physics, Materials, and Applications. *Sensors* **2022**, *22*, 820. [CrossRef] [PubMed]
8. Kinyua, C.K.; Owino, A.O.; Kaur, K.; Das, D.; Karuri, N.W.; Müller, M.; Schönherr, H. Impact of Surface Area on Sensitivity in Autonomously Reporting Sensing Hydrogel Nanomaterials for the Detection of Bacterial Enzymes. *Chemosensors* **2022**, *10*, 299. [CrossRef]
9. Enesca, A.; Isac, L. Tandem Structures Semiconductors Based on TiO_2_SnO_2 and ZnO_SnO_2 for Photocatalytic Organic Pollutant Removal. *Nanomaterials* **2021**, *11*, 200. [CrossRef]
10. Piątkowska, A.; Janus, M.; Szymański, K.; Mozia, S. C-,N- and S-Doped TiO_2 Photocatalysts: A Review. *Catalysts* **2021**, *11*, 144. [CrossRef]
11. Kang, X.; Liu, S.; Dai, Z.; He, Y.; Song, X.; Tan, Z. Titanium dioxide: From engineering to applications. *Catalysts* **2019**, *9*, 191. [CrossRef]
12. Rajput, R.B.; Jamble, N.S.; Kale, R.B. A review on TiO_2/SnO_2 heterostructures as a photocatalyst for the degradation of dyes and organic pollutants. *J. Environ. Manag.* **2022**, *307*, 114533. [CrossRef]
13. Zhu, H.; Tan, J.; Qiu, J.; Wang, D.; Zhao, Z.; Lu, Z.; Huang, G.; Liu, X.; Mei, Y. Gold Nanoparticles Decorated Titanium Oxide Nanotubes with Enhanced Antibacterial Activity Driven by Photocatalytic Memory Effect. *Coatings* **2022**, *12*, 1351. [CrossRef]
14. Ali, F.; Moin-ud-Din, G.; Iqbal, M.; Nazir, A.; Altaf, I.; Alwadai, N.; Siddiqua, U.H.; Younas, U.; Ali, A.; Kausar, A.; et al. Ag and Zn doped TiO_2 nano-catalyst synthesis via a facile green route and their catalytic activity for the remediation of dyes. *J. Mater. Res. Technol.* **2023**, *23*, 3626–3637. [CrossRef]
15. Sohail, I.; Bhatti, I.A.; Ashar, A.; Sarim, F.M.; Mohsin, M.; Naveed, R.; Yasir, M.; Iqbal, M.; Nazir, A. Polyamidoamine (PAMAM) dendrimers synthesis, characterization and adsorptive removal of nickel ions from aqueous solution. *J. Mater. Res. Technol.* **2020**, *9*, 498–506. [CrossRef]
16. Naseer, A.; Ali, A.; Ali, S.; Mahmood, A.; Kusuma, H.S.; Nazir, A.; Yaseen, M.; Khan, M.I.; Ghaffar, A.; Abbas, M.; et al. Biogenic and eco-benign synthesis of platinum nanoparticles (Pt NPs) using plants aqueous extracts and biological derivatives: Environmental, biological and catalytic applications. *J. Mater. Res. Technol.* **2020**, *9*, 9093–9107. [CrossRef]
17. Scarisoreanu, M.; Ilie, A.G.; Goncearenco, E.; Banici, A.M.; Morjan, I.P.; Dutu, E.; Tanasa, E.; For, I.; Stan, M.; Mihailescu, C.N.; et al. Ag, Au and Pt decorated TiO_2 biocompatible nanospheres for UV & vis photocatalytic water treatment. *Appl. Surf. Sci.* **2020**, *509*, 145217.
18. Scarisoreanu, M.; Fleaca, C.; Morjan, I.; Niculescu, A.-M.; Luculescu, C.; Dutu, E.; Ilie, A.; Morjan, I.; Gavrila Florescu, L.; Vasile, E.; et al. High photoactive TiO_2/SnO_2 nanocomposites prepared by laser pyrolysis. *Appl. Surf. Sci.* **2017**, *418*, 491–498. [CrossRef]
19. Ali, F.; Khan, S.B.; Asiri, A.M. Enhanced H_2 generation from $NaBH_4$ hydrolysis and methanolysis by cellulose micro-fibrous cottons as metal templated catalyst. *Int. J. Hydrogen Energy* **2018**, *43*, 6539–6550. [CrossRef]
20. Spurr, R.A.; Myers, H. Quantitative Analysis of Anatase-Rutile Mixtures with an X-Ray Diffractometer. *Anal. Chem.* **1957**, *29*, 760–762. [CrossRef]

21. Hanaor, D.A.H.; Chironi, I.; Karatchevtseva, I.; Triani, G.; Sorrell, C.C. Single and mixed phase TiO_2 powders prepared by excess hydrolysis of titanium alkoxide. *Adv. Appl. Ceram.* **2012**, *111*, 149–158. [CrossRef]
22. Takahashi, K.; Kunz, A.; Woiki, D.; Roth, P. Thermal Decomposition of Tin Tetrachloride Based on Cl- and Sn-Concentration Measurements. *J. Phys. Chem. A* **2000**, *104*, 5246–5253. [CrossRef]
23. Scherrer, P. Nachrichten von der Gesellschaft der Wissenschaften zu Göttingen. *Math.-Phys. Kl.* **1918**, *2*, 98–100.
24. Cho, H.-W.; Liao, K.-L.; Yang, J.-S.; Wu, J.-J. Revelation of rutile phase by Raman scattering for enhanced photoelectrochemical performance of hydrothermally-grown anatase TiO_2 film. *Appl. Surf. Sci.* **2018**, *440*, 125–132. [CrossRef]
25. Makal, P.; Das, D. Self-doped TiO_2 nanowires in TiO_2-B single phase, TiO_2-B/anatase and TiO_2-anatase/rutile heterojunctions demonstrating individual superiority in photocatalytic activity under visible and UV light. *Appl. Surf. Sci.* **2018**, *455*, 1106–1115. [CrossRef]
26. Islam, S.K.; Lombardi, J.R. Raman enhancement (SERS) of the surface phonon modes of TiO_2. *Chem. Phys. Lett.* **2022**, *806*, 140040. [CrossRef]
27. Wehinger, B.; Bosak, A.; Jochym, P. Soft phonon modes in rutile TiO_2. *Phys. Rev. B* **2016**, *93*, 014303. [CrossRef]
28. Nurkowski, D.; Jasper, A.W.; Akroyd, J.; Kraft, M. Theoretical Study of the Ti–Cl Bond Cleavage Reaction in $TiCl_4$. *Z. Phys. Chem.* **2017**, *231*, 1489–1506. [CrossRef]
29. De Buysser, K.; Van Driessche, I.; Van de Putte, B.; Vanhee, P.; Schaubroeck, J.; Hoste, S. Study of Negative Thermal Expansion and Shift in Phase Transition Temperature in Ti4+- and Sn4+ -Substituted ZrW_2O_8 Materials. *Inorg. Chem.* **2008**, *47*, 736–741. [CrossRef]
30. Liu, D.; Pan, J.; Tang, J.; Liu, W.; Bai, S.; Luo, R. Ag decorated SnO_2 nanoparticles to enhance formaldehyde sensing properties. *J. Phys. Chem. Solids* **2019**, *124*, 36–43. [CrossRef]
31. Bhardwaj, N.; Satpati, B.; Mohapatra, S. Plasmon-enhanced photoluminescence from SnO_2 nanostructures decorated with Au nanoparticles. *Appl. Surf. Sci.* **2020**, *504*, 144381. [CrossRef]
32. Chen, Y.; Zhu, B.; Yao, M.; Wang, S.; Zhang, S. The preparation and characterization of Au@TiO_2 nanoparticles and their catalytic activity for CO oxidation. *Catal. Commun.* **2010**, *11*, 1003–1007. [CrossRef]
33. Firet, N.J.; Blommaert, M.A.; Burdyny, T.; Venugopal, A.; Bohra, D.; Longo, A.; Smith, W.A. Operando EXAFS study reveals presence of oxygen in oxide-derived silver catalysts for electrochemical CO_2 reduction. *J. Mater. Chem. A* **2019**, *7*, 2597–2607. [CrossRef]
34. Li, H.; Bian, Z.; Zhu, J.; Huo, Y.; Li, H.; Lu, Y. Mesoporous Au/TiO_2 Nanocomposites with Enhanced Photocatalytic Activity. *J. Am. Chem. Soc.* **2007**, *129*, 4538–4539. [CrossRef] [PubMed]
35. Fabregat-Santiago, F.; Mora-Sero, I.; Garcia-Belmonte, G.; Bisquert, J. Cyclic Voltammetry studies of nanoporous semiconductors. Capacitive and reactive properties of nanocrystalline TiO_2 electrodes in aqueous electrolyte. *J. Phys. Chem. B* **2003**, *107*, 758. [CrossRef]
36. Lopez, R.; Gomez, R. Band-gap energy estimation from diffuse reflectance measurements on sol–gel and commercial TiO_2: A comparative study. *J. Sol-Gel Sci. Technol.* **2012**, *61*, 1–7. [CrossRef]
37. Pelant, I.; Valenta, J. *Luminescence of Excitons, Luminescence Spectroscopy of Semiconductors*; Oxford University Press: Oxford, UK, 2012; Volume 7, pp. 161–204.
38. Mercado, C.C.; Knorr, F.J.; McHale, J.L.; Usmani, S.M.; Ichimura, A.S.; Saraf, L.V. Location of Hole and Electron Traps on Nanocrystalline Anatase TiO_2. *J. Phys. Chem. C* **2012**, *116*, 10796–10804. [CrossRef]
39. Ghamsari, M.S.; Gaeeni, M.R.; Han, W.; Park, H.-H. Highly stable colloidal TiO_2 nanocrystals with strong violet-blue emission. *J. Lumin.* **2016**, *178*, 89–93. [CrossRef]
40. Jing, L.; Xin, B.; Yuan, F.; Xue, L.; Wang, B.I.; Fu, H. Effects of Surface Oxygen Vacancies on Photophysical and Photochemical Processes of Zn-Doped TiO_2 Nanoparticles and Their Relationships. *J. Phys. Chem. B* **2006**, *110*, 17860–17865. [CrossRef]
41. Dirac, P.A.M. On the theory of quantum mechanics. *Proc. R. Soc. Lond. A* **1926**, *112*, 661–677.
42. Zhang, L.; Dai, L.; Li, X.; Yu, W.; Li, S.; Guan, J. 3D structured TiO2 based aerogel photocatalyst for the high-efficiency degradation of toluene gas. *New J. Chem.* **2022**, *46*, 2272–2281. [CrossRef]
43. Kaur, R.; Pal, B. Plasmonic coinage metal–TiO_2 hybrid nanocatalysts for highly efficient photocatalytic oxidation under sunlight irradiation. *New J. Chem.* **2015**, *39*, 5966–5976. [CrossRef]
44. Choi, H.; Carboni, M.; Kim, Y.K.; Jung, C.H.; Moon, S.Y.; Koebel, M.M.; Parl, J.Y. Synthesis of High Surface Area TiO2 Aerogel Support with Pt Nanoparticle Catalyst and CO Oxidation Study. *Catal. Lett.* **2018**, *148*, 1504–1513. [CrossRef]
45. Deriase, S.F.; El-Salamony, R.A.; Amdeha, E.; Al-Sabagh, A.M. Statistical optimization of photocatalytic degradation process of methylene blue dye by SnO–TiO_2–AC composite using response surface methodology. *Environ. Prog. Sustain. Energy* **2021**, *40*, e13639. [CrossRef]
46. Dong, Z.; Wu, M.; Wu, J.; Ma, Y.; Ma, Z. In situ synthesis of TiO_2/SnOx-Au ternary heterostructures effectively promoting visible light photocatalysis. *Dalton Trans.* **2015**, *44*, 11901–11910. [CrossRef] [PubMed]

47. Prakash, J.; Sun, S.; Swart, H.C.; Gupta, R.K. Noble metals-TiO_2 nanocomposites: From fundamental mechanisms to photocatalysis, surface enhanced Raman scattering and antibacterial applications. *Appl. Mater. Today* **2018**, *11*, 82–135. [CrossRef]
48. Ramos, D.; Almeida, L. Overview of Standards Related to the Occupational Risk and Safety of Nanotechnologies. *Standards* **2022**, *2*, 83–89. [CrossRef]